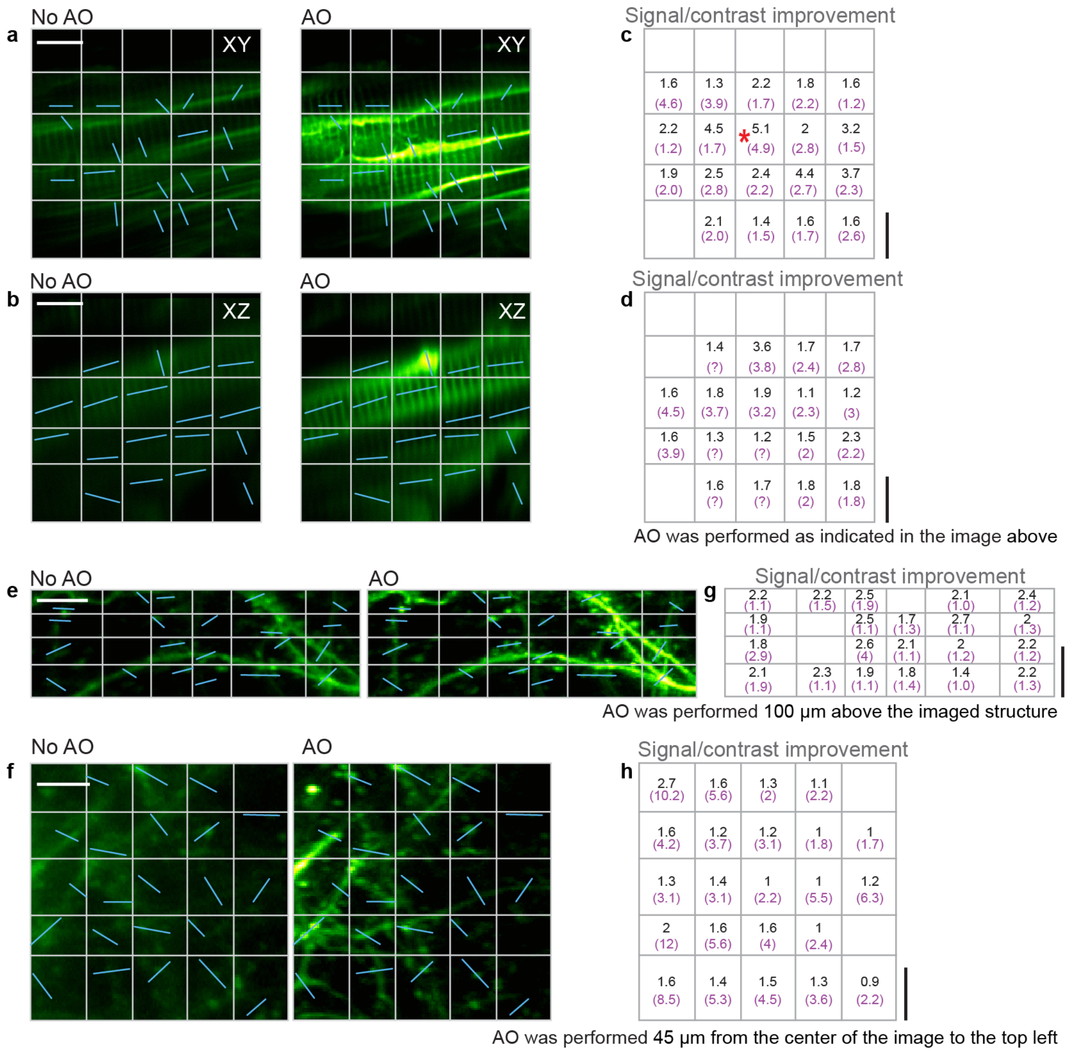

c Signal/contrast improvement

1.6 (4.6)	1.3 (3.9)	2.2 (1.7)	1.8 (2.2)	1.6 (1.2)
2.2 (1.2)	4.5 (1.7)	* 5.1 (4.9)	2 (2.8)	3.2 (1.5)
1.9 (2.0)	2.5 (2.8)	2.4 (2.2)	4.4 (2.7)	3.7 (2.3)
	2.1 (2.0)	1.4 (1.5)	1.6 (1.7)	1.6 (2.6)

d Signal/contrast improvement

	1.4 (?)	3.6 (3.8)	1.7 (2.4)	1.7 (2.8)
1.6 (4.5)	1.8 (3.7)	1.9 (3.2)	1.1 (2.3)	1.2 (3)
1.6 (3.9)	1.3 (?)	1.2 (?)	1.5 (2)	2.3 (2.2)
	1.6 (?)	1.7 (?)	1.8 (2)	1.8 (1.8)

AO was performed as indicated in the image above

g Signal/contrast improvement

2.2 (1.1)	2.2 (1.5)	2.5 (1.9)		2.1 (1.0)	2.4 (1.2)
1.9 (1.1)		2.5 (1.1)	1.7 (1.3)	2.7 (1.1)	2 (1.3)
1.8 (2.9)		2.6 (4)	2.1 (1.1)	2 (1.2)	2.2 (1.2)
2.1 (1.9)	2.3 (1.1)	1.9 (1.1)	1.8 (1.4)	1.4 (1.0)	2.2 (1.3)

AO was performed 100 µm above the imaged structure

h Signal/contrast improvement

2.7 (10.2)	1.6 (5.6)	1.3 (2)	1.1 (2.2)	
1.6 (4.2)	1.2 (3.7)	1.2 (3.1)	1 (1.8)	1 (1.7)
1.3 (3.1)	1.4 (3.1)	1 (2.2)	1 (5.5)	1.2 (6.3)
2 (12)	1.6 (5.6)	1.6 (4)	1 (2.4)	
1.6 (8.5)	1.4 (5.3)	1.5 (4.5)	1.3 (3.6)	0.9 (2.2)

AO was performed 45 µm from the center of the image to the top left

Supplementary Figure 1 | Signal and contrast improvement for the images shown in Fig. 1 of the article. **a**,**b**, 2P images of myotomes in zebrafish larva. **c**,**d**, Improvement in signal (black fonts) and contrast (purple fonts) across field of view for the images shown in **a** and **b**, respectively. **e**,**f**, 2P images of neurites in the mouse brain. **g**,**h**, Improvement in signal (black fonts) and contrast (purple fonts) across field of view for the images shown in **e** and **f**, respectively. Red star indicates location where AO was performed. Question mark indicates contrast could not be calculated in the No AO image. Scale bars: 10 µm in **a**-**d** and 5 µm in **e**-**h**.

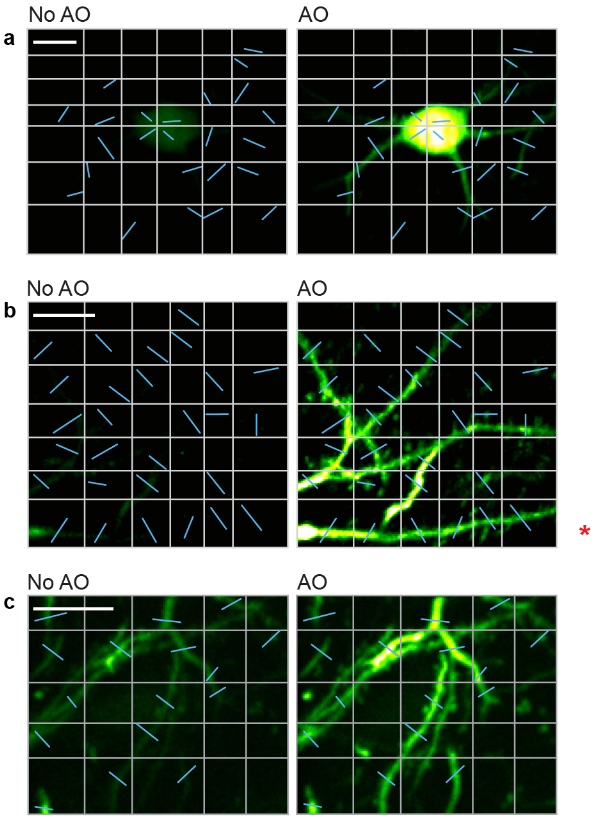

d Signal improvement

					8
					18
	?			21	17
14	19	6	6	12	18
	9	7	* 8		19
16	19		10	13	14
		?	12	14	?

e Signal improvement

			9		
8	8	9	8		
11	18	10		?	10
19	17		29	17	16
13	19	16			
13	15	15		10	
14	9	11	?	?	30

f Signal improvement

1.3		3.4	1.75	
2	2.6	3.5	3.1	1.8
2.7		4.6	4	
2.2		7		
1.2	5.6	7		

AO was performed ~14 µm above these dendrites,
on cell body shown in Fig 2f (main manuscript)

Supplementary Figure 2 | Signal improvement for the images shown in Fig. 2 of the article. **a**,**b**, 3P images of the mouse cortex and **c,** hippocampus. **d**,**e**,**f**, Improvement in signal (black fonts) across field of view, for the images shown in **a**, **b**, and **c**, respectively. Red star indicates location where AO was performed. Question mark indicates structure was below noise level in the No AO image. Scale bars, 10 µm.

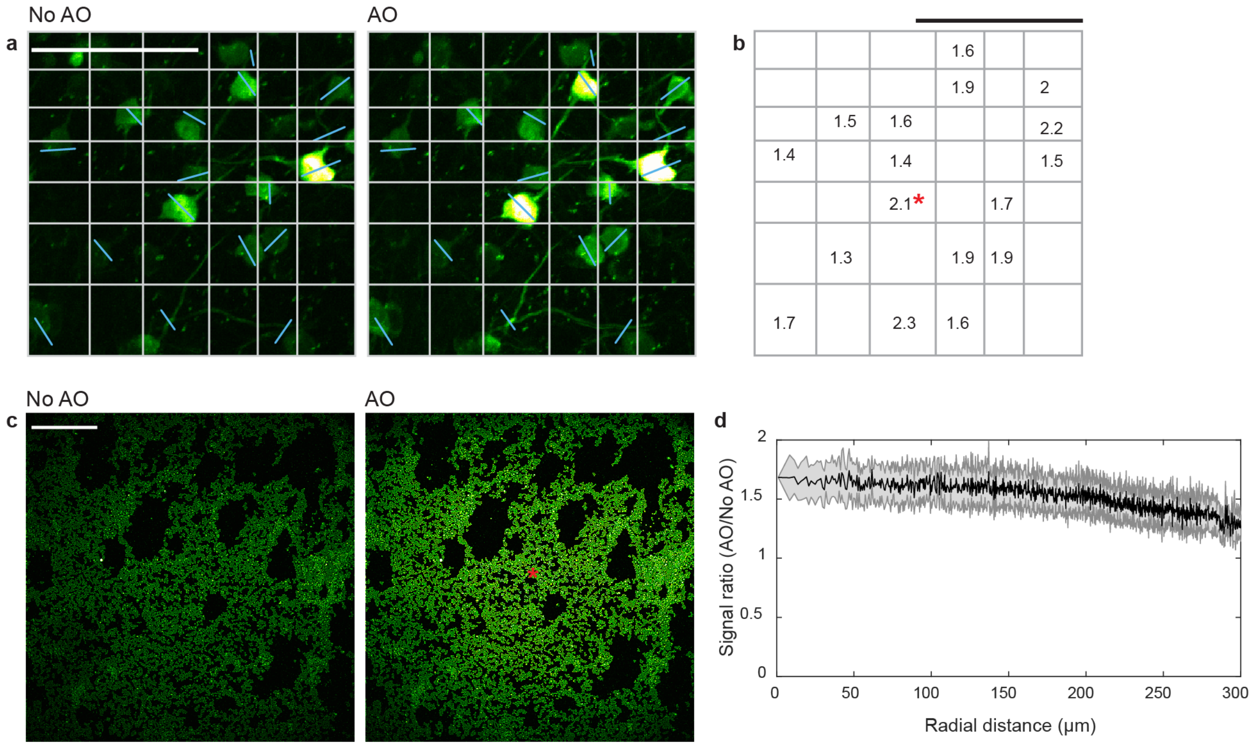

Supplementary Figure 3 | 3P signal improvement throughout fields of view up to 400 μm. **a**, 3P images before and after AO correction (200×200 μm field of view) obtained during *in vivo* 3P imaging of GCaMP6-labeled neurons in layer 6 of the mouse brain (681 μm below dura). **b**, Improvement in signal across the field of view after aberration correction. The signal improvement was observed throughout the field of view, ranging between 1.3-2.3×. **c**, 3P images before and after AO correction (500×500 μm field of view) obtained during 3P imaging of 2-μm diameter fluorescent beads under a #1.5 coverglass. **d**, Improvement in 3P signal after aberration correction as a function of the radial distance, with the origin being the center of the image (where AO was performed). The signal improvement was within 8% of optimal performance over a field of view of 400 μm. Shaded area: s.e.m. Red star indicates location where AO was performed. Scale bars, 100 μm.

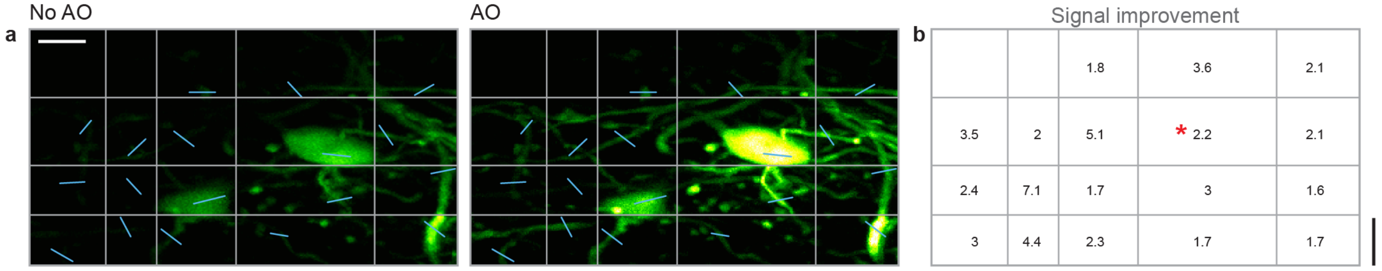

Supplementary Figure 4 | Signal improvement for the images shown in Fig. 3 of the article. **a**, 3P images of the mouse spinal cord. **b**, Improvement in signal (black fonts) across field of view. Red star indicates location where AO was performed. Scale bars, 10 μm.

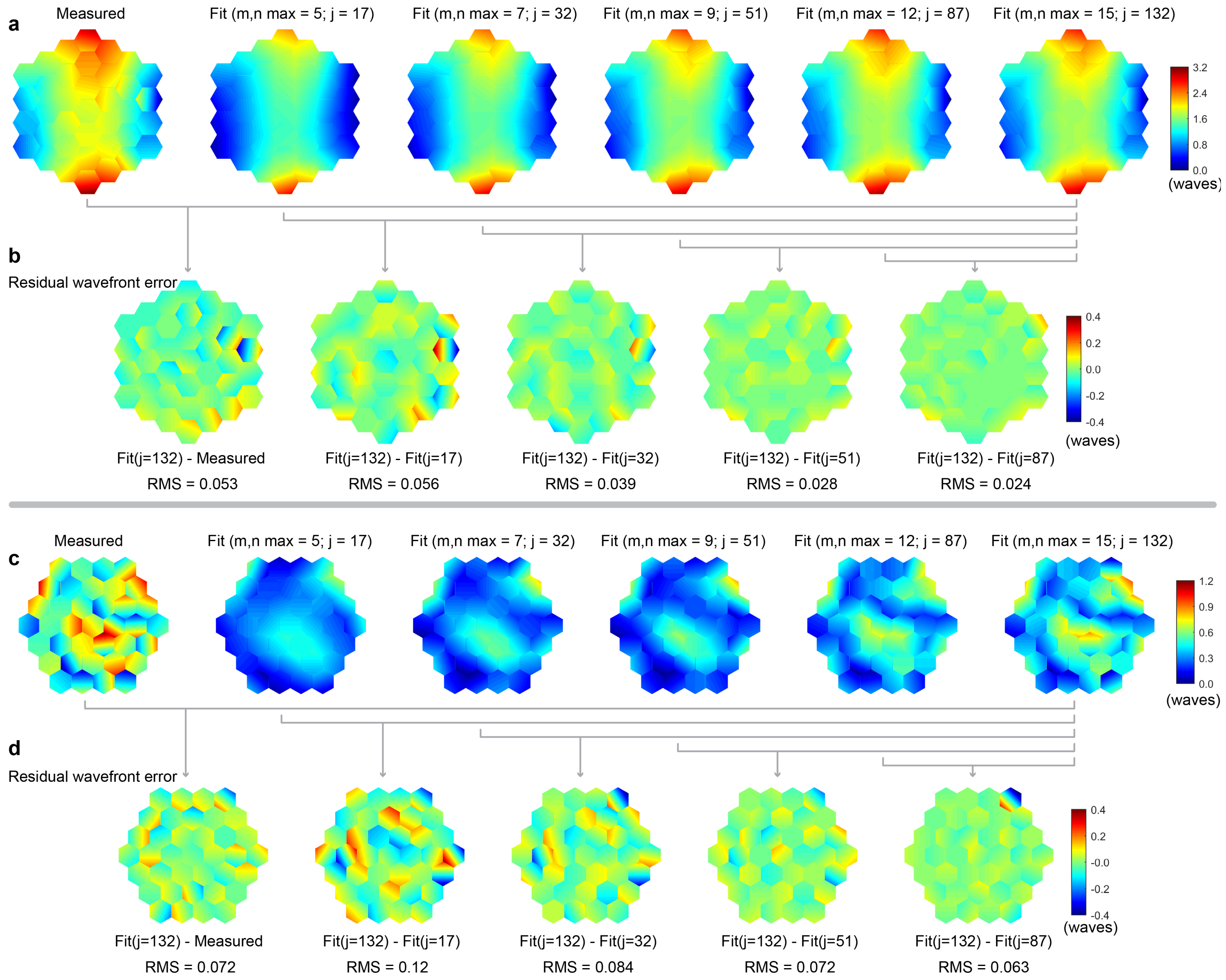

Supplementary Figure 5 | Comparison of our zonal wavefront correction method and modal approaches for representative smooth and complex aberrations. **a**, Corrective wavefronts in Fig. 1c (representative of smooth wavefronts) and Fig. 3g (representative of complex wavefronts) (leftmost panels), and their fitted wavefronts using Zernike polynomials (n,m) up to 5th, 7th, 9th, 12th, and 15th order (right) – corresponding to j = 17, 32, 51, 87, and 132 Zernike modes, respectively, not including tip, tilt, or piston. The wavefronts that are fitted using up to 15th order are used as the ground-truth corrective wavefront. **b**, Residual wavefronts calculated by subtracting from the ground-truth wavefronts the experimentally measured corrective wavefront (leftmost panels), as well as the fitted wavefronts using Zernike polynomials up to 5th, 7th, 9th, and 12th order. **c**, Corrective wavefronts in Fig. 3g (representative of complex wavefronts) (leftmost panels), and their fitted wavefronts using Zernike polynomials (n,m) up to 5th, 7th, 9th, 12th, and 15th order (right). **d**, Residual wavefronts calculated by subtracting from the ground-truth wavefronts the experimentally measured corrective wavefront (leftmost panels), as well as the fitted wavefronts using Zernike polynomials up to 5th, 7th, 9th, and 12th order. RMS: root-mean square for each residual wavefront.

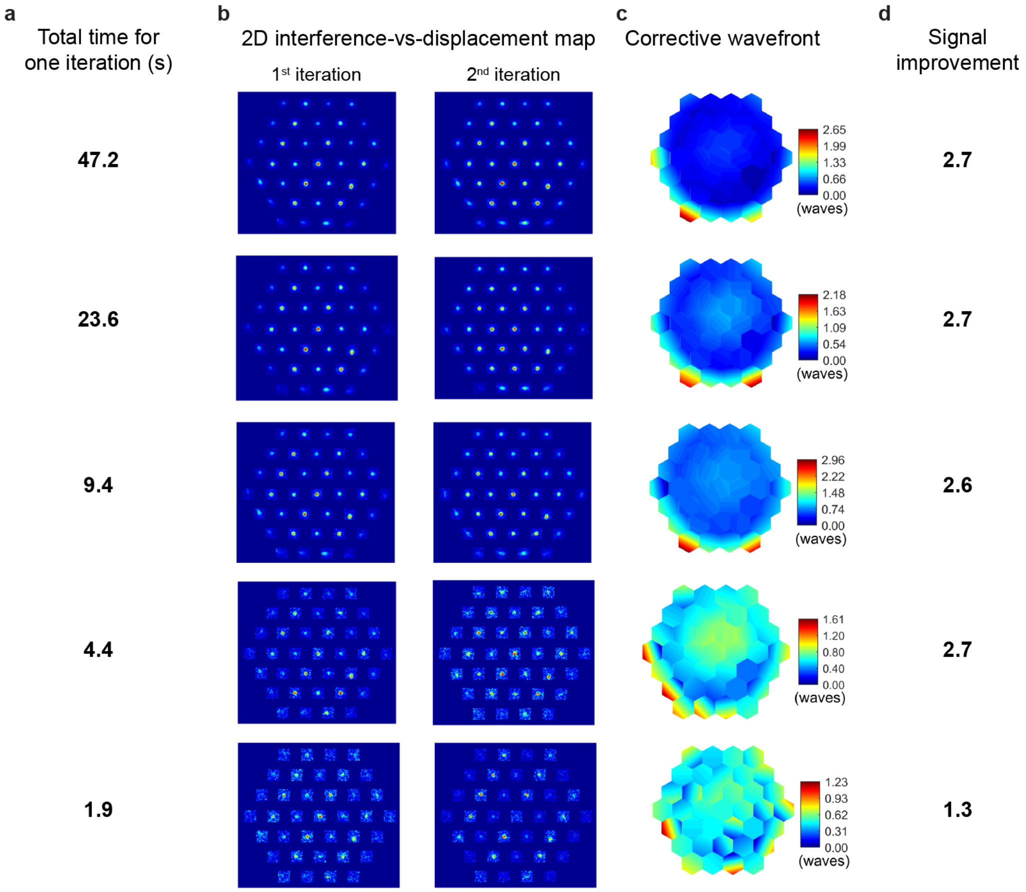

Supplementary Figure 6 | Comparison of aberration correction performance using different integration times, for 2-μm diameter beads placed under a #1.5 coverglass. **a**, Total fluorescence acquisition times. **b**, 2D interference-vs-displacement map for each of the 2 iterations performed. **c**, Final corrective wavefront. **d**, Signal improvement found in each case. Note that, for this aberration, most improvement resulted from the 1st iteration, with the 2nd iteration leading to <30% improvement in signal over the 1st iteration. See Supplementary Table 3 for more details.

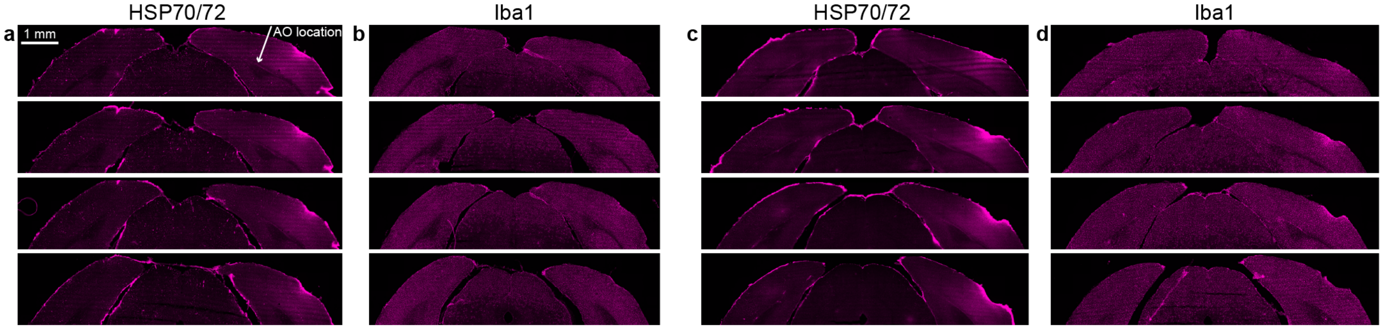

Supplementary Figure 7 | Assessment of tissue damage on the mouse brain. **a**,**b**, Mouse brain slices (wild-type mouse; C57BL/6J) immunolabeled against heat shock protein (HSP70/72) and microglial activation (Iba1), respectively (see Supplementary Note 4 for details). AO routine was performed 750 µm below dura (white arrow). Three iterations were performed (phase modulation), with an overall fluorescence acquisition time of 23.6 s per iteration. Average powers: 30, 20, and 18 mW for the 1st, 2nd, and 3rd iterations, respectively, of the phase gradient measurement step; and 17, 13, and 13 mW for the 1st, 2nd, and 3rd iterations, respectively, of the phase offset measurement step. **c**,**d**, Mouse brain slices immunolabeled against HSP70/72 and Iba1, respectively, for control mouse. The control mouse (same age and sex as experimental mouse) had undergone the same cranial window implantation procedure on the same day as the experimental mouse but was never exposed to laser light. Note that while activated microglia can result from physiological stress to the brain, including inflammation, the overexpression of heat shock proteins is known to increase resistance and protection against a wide range of stressful conditions including heat, inflammation, oxidative stress, and infections. Three weeks after window implantation, the surfaces of the brain exposed to laser light through our AO routine (**a**,**b**) and the control brain (**c**,**d**) showed similar signs of immunoreactivity to HSP and Iba1. Given the superficial locations of the immunoreactive regions and their similarity in strength, we attribute such responses to the window implantation procedure and not to the laser exposure during AO routine (arrow in panel **a**, 750 µm below brain surface). n = 1 mouse for **a** and **b**, respectively.

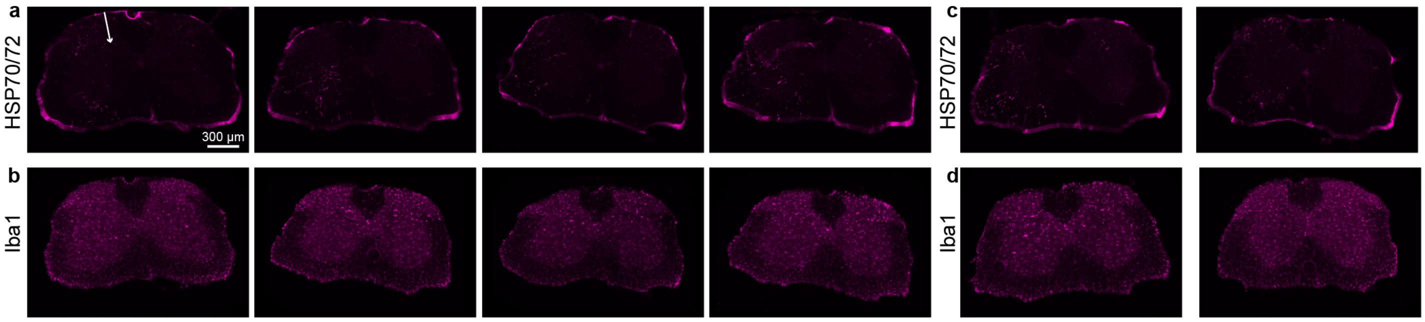

Supplementary Figure 8 | Assessment of tissue damage on the mouse spinal cord. **a**,**b**, Mouse spinal cord slices (wild-type mouse; C57BL/6J) immunolabeled against heat shock protein (HSP70/72) and microglial activation (Iba1), respectively (see Supplementary Note 4 for details). AO routine was performed 300 µm below dura (white arrow indicates depth). Two iterations were performed (phase modulation), with an overall fluorescence acquisition time of 23.6 s per iteration. Average powers: 30 mW for the 1st and 2nd iterations of the phase gradient measurement step; and 17 mW for the 1st and 2nd iterations of the phase offset measurement step. No difference in immunoreactivity is found between the right and left sides of the spinal cord. **c**,**d**, Mouse spinal cord slices – rostral to where the window was implanted (1-2 mm away from the laser-exposed area) – immunolabeled against HSP70/72 and Iba1, respectively. Similar immunoreactivity to HSP and Iba1 was found in the spinal cord slices exposed to laser light (**a**,**b**) when compared to those not exposed to laser light (**c**,**d**). n = 1 mouse.

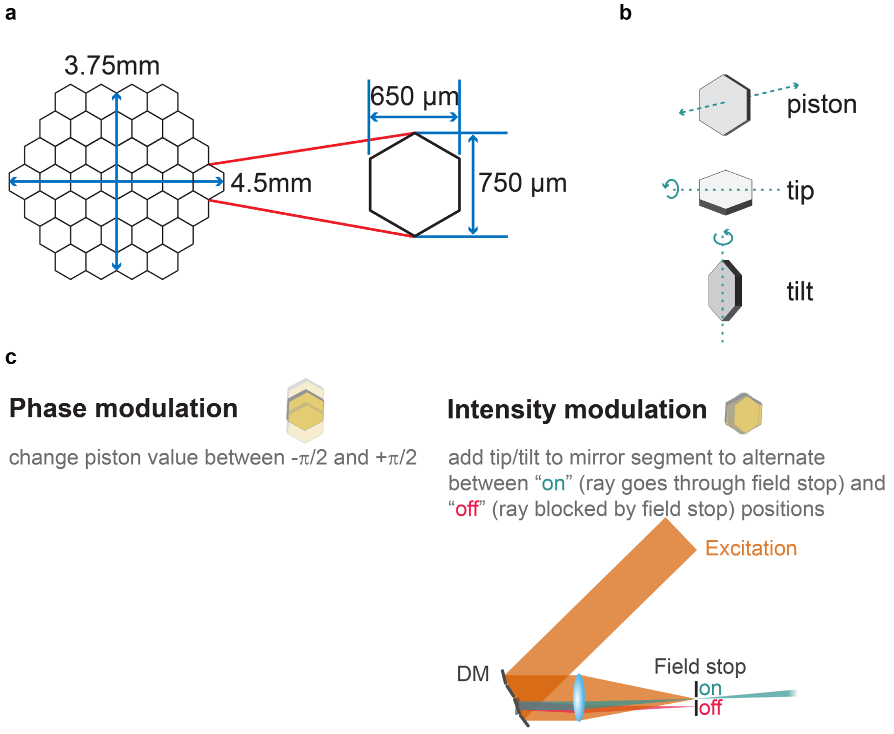

Supplementary Figure 9 | Deformable mirror (DM) specifications. **a**, Diagram of the hexagonal segmented DM (Boston Micromachines Corporation) consisting of 37 segments and a 3.8-mm-diameter clear aperture. **b**, Each segment is controlled by three actuators to provide an angular control of approximately ± 3 mrad in tip and tilt, and a maximum axial stroke (piston displacement) of 3.5 µm. **c**, Diagram showing the two modulation strategies used by our aberration measurement method. See Online Methods for details.

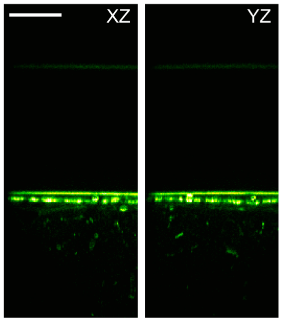

Supplementary Figure 10 | Cranial window alignment using the third-harmonic signal generated at the glass window - brain interface. Axial third-harmonic generation images of a cranial window above a Thy1-YFP-H mouse brain *in vivo*. Both the 3P fluorescence and the third-harmonic signals are shown, where the third-harmonic signal generated at the interfaces of the coverglass are clearly distinguished. Excitation wavelength: 1300 nm (same imaging session as in Fig. 2 a-d). Post-objective power: 2 mW. Scale bar, 50 µm. Microscope objective: NA 1.05 25×. Representative results from n>20 mice.

Supplementary Tables

Fig.	Imaging depth (μm)	Post-objective power (mW)	Excitation wavelength (nm)	AO rounds	Modulation strategy	Pixel size (μm)	Mouse line/age/acute or chronic imaging
1 a	110	13	920	4	phase	0.1	zebrafish line: Tg(β-actin:HRAS-EGFP)
1 d	365-375	31	920	3	phase	0.15	Thy1-YFP-H/>30wks/acute
1 g	490-513	128	920	3	phase	0.2	Thy1-YFP-H/>30wks/acute
2 a	747-767	17	1300	3	phase	0.2	Thy1-YFP-H/6wks/acute
2 b	751-767	20	1300	3	phase	0.15	Thy1-YFP-H/6wks/acute
2 f	719	16	1300	3	phase	0.2	Thy1-YFP-H/>30wks/chronic
2 g	695-709	26	1300	3	phase	0.12	Thy1-YFP-H/>30wks/chronic
2 k	952	30	1700	3	phase	0.2	Gad2-IRES-Cre Jax X Ai14/>30wks/chronic
3 b	208-228	18.3	1300	2	phase	0.25	Thy1-GFP-M/10wks/acute
3 e	414	89	1300	3	phase	0.5	Thy1-GFP-M/9wks/acute
3 i	310	4.2	1300	2	phase	0.5	AAV8-Syn-jGCaMP7s/5wks/acute
Extended Data Fig.	**Imaging depth (μm)**	**Post-objective power (mW)**	**Excitation wavelength (nm)**	**AO rounds**	**Modulation strategy**	**Pixel size (μm)**	**Mouse line/age/acute or chronic imaging**
1 c	N/A	0.13	1300	1	phase	0.05	N/A
2 c	N/A	6	920	3	phase	0.05	N/A
2 d	N/A	2.3	920	4	phase	0.25	N/A
3 a,c	Same images as in Fig. 1d,g						
4 b	N/A	0.13	1300	4	phase	0.05	N/A
5 a	757	17	1300	3	phase	0.2	Thy1-YFP-H/6wks/acute
5 d	747-757	20	1300	3	phase	0.12	Thy1-YFP-H/6wks/acute
5 e	687	35	1300	2	phase	0.25	Thy1-GFP-M/>30wks/acute
5 h	624-644	13	1300	2	phase	0.25	Thy1-GFP-M/5wks/acute
6 a	623	20.8	1300	5	phase	0.2	Thy1-YFP-H/>30wks/chronic
6 d	623	23.6	1300	5	intensity	0.2	Thy1-YFP-H/>30wks/chronic
7 a	601-616	17	1300	4	phase	0.2	Thy1-YFP-H/>30wks/chronic
7 d	609-619	25.6	1300	4	phase	0.15	Thy1-YFP-H/>30wks/chronic
7 h	863-875	42	1300	2	phase	0.2	Thy1-YFP-H/5wks/acute
8 a	917	26.5	1700	3	phase	0.2	Gad2-IRES-Cre × Ai14/>30wks/chronic
8 d	960	10	1700	3	phase	0.2	AAV-Syn-Cre + AAV-CAG-FLEX-tdTomato/11wks/acute
8 g	1010	27	1700	3	phase	0.2	AAV-Syn-Cre + AAV-CAG-FLEX-tdTomato/11wks/acute
8 j	1020	24	1700	3	phase	0.2	AAV-Syn-Cre + AAV-CAG-FLEX-tdTomato/11wks/acute
9	N/A						

Supplementary Table 1 | Experimental parameters used for the aberration measurement data shown in this work.

	fit (n,m=15; j=132) - Measured (our method)	fit (n,m=15; j=132) - fit (n,m=5; j=17)	fit (n,m=15; j=132) - fit (n,m=7; j=32)	fit (n,m=15; j=132) - fit (n,m=9; j=51)	fit (n,m=15; j=132) - fit (n,m=12; j=87)
	RMS zonal (waves)	**RMS modal (waves)**			
Fig. 1c	0.053	0.056	**0.039**	0.028	0.024
Fig. 1f	0.089	0.12	**0.072**	0.048	0.033
Fig. 1i	0.11	0.14	**0.095**	0.056	0.045
Fig. 2d	0.042	0.067	0.050	**0.036**	0.019
Fig. 2h	0.060	0.090	**0.060**	0.034	0.027
Fig. 2k	0.071	0.13	0.099	**0.062**	0.051
Fig. 3d	0.035	0.052	**0.030**	0.024	0.018
Fig. 3g	0.072	0.12	0.084	**0.072**	0.063
Fig. 3k	0.052	0.082	0.063	**0.043**	0.038

Supplementary Table 2 | Comparison of our zonal wavefront correction method and modal approaches for the corrective wavefronts shown in the main figures of the article. Root-mean square (RMS) errors of the residual wavefronts obtained using our zonal method (1st column) and modal methods using Zernike polynomials (n,m) up to 5th, 7th, 9th, 12th, and 15th order (later columns) – corresponding to j = 17, 32, 51, 87, and 132 Zernike modes, respectively, not including tip, tilt, or piston. The wavefronts that are fitted using up to 15th order are used as the ground-truth corrective wavefront. The RMS error for each residual wavefront was calculated by subtracting from the ground-truth wavefronts the experimentally measured corrective wavefront (1st column), as well as the fitted wavefronts using Zernike polynomials up to 5th, 7th, 9th, and 12th order (later columns). RMS values in bold indicate a similar or lower RMS error than that obtained with our wavefront correction approach. n,m: order of fit to Zernike polynomials. j: total number of Zernike functions used in the fit (excluding tip, tilt, and piston). See Supplementary Fig. 5 showing two example corrective wavefronts: a relatively smooth one (from Fig. 1c), for which our approach yields similar wavefront errors as modal correction up to 7th order; and a more complex one (Fig. 3g), for which our approach yields similar wavefront errors as modal correction up to 9th order.

Signal improvement	Integration time (ms)		Total time for one iteration (s)
	$T_{gradient}$	T_{phase}	
2.7	180	360	47.2
2.7	90	180	23.6
2.6	36	72	9.4
2.7	10.8	180	4.4
1.3	7.2	14.4	1.9

Supplementary Table 3 | Comparison of aberration correction performance using different integration times, for 2-µm diameter beads placed under a #1.5 coverglass. Summary of the results presented in Supplementary Fig. 6 specifying the signal improvement found for each integration time, the integration time used for the phase gradient and phase offset measurement steps, as well as the total fluorescence acquisition time: $2 \times n \times n \times T_{gradient} + 2 \times 5 \times T_{phase}$. Here, $T_{gradient}$ and T_{phase} are the integration times used for the phase gradient and phase offset measurement steps of our aberration measurement procedure, respectively; $n \times n$ is the total number of tip and tilt angles (typical value used: n = 11); the factor of 2 comes from splitting the total number of DM segments into two groups; and the factor of 5 refers to the total number of iterations performed during the phase offset step. Row highlighted in green indicates typical parameters used for the data shown in our manuscript.

Supplementary Notes

Supplementary Note 1: Deformable mirror (DM) specifications, calibration, and verification procedure

The deformable mirror in this project is a hexagonal tip-tilt-piston DM (Hex-111-X) manufactured by Boston Micromachines Corporation (Supplementary Fig. 9). The device features 37 hexagonal segments, each anchored to three electrostatic actuators by short attachment posts, a 3.8-mm-diameter clear aperture, and a protective window with anti-reflection coating (400 nm to 1100 nm for 2P experiments and 550 nm to 2400 nm for 3P experiments). We developed it for microscopy application from a 331-segment tip-tilt-piston mirror array originally designed for space-based AO[1,2]. The actuators are independently addressable and can achieve a maximum of 3.5 μm of surface-normal stroke for an input voltage of ~200 V. Tip, tilt, and piston control of mirror segments is achieved by applying command voltages to each of the three actuators. The electromechanical system has no measurable hysteresis. The maximal segment piston motion achievable is 3.5 μm, and the maximal tip and tilt angle achievable is ± 5.7 mrad. However, these maxima are not independent. The range of tip and tilt angle achievable depends on the nominal piston value, and vice versa. Coupling forces and torques are generated on the actuators through their mechanical connection to the mirror segment. As a result, the surface normal deflection at a given actuator post depends not only on the voltage applied to that actuator, but also on the state of its neighboring actuators. Nevertheless, there is a one-to-one mapping between the voltages applied to the three actuators and the resulting tip, tilt, and piston orientations of the segment.

A calibration process was used to fit a mathematical model to that mapping. During calibration, the tip, tilt, and piston of each segment was measured to nanometer-scale precision using a surface mapping interferometer (Zygo 6100) in response to each of 2744 input voltage states applied to the actuators (with voltages ranging from 0 V to 200 V in 14 steps for each actuator). A least squares fourth order polynomial fit was made between the input state (the vector comprised of the three actuator input voltages) and the output state (the vector comprised of the three segment orientations, tip, tilt, and piston). The correlation coefficient of the fit was 1.000. This fit was used to create a lookup table that could be interpolated to map any desired output orientation to a corresponding triplet of required actuator input voltages. The calibration was tested in the interferometer, and yielded precision corresponding to approximately 1 nm in piston motion and 0.1 μradians in tip and tilt.

The calibration of the DM was further tested in our microscope setup. Piston displacement was verified by recording the fluorescence signal from a 1-μm diameter fluorescent bead while piston displacing one mirror segment. A sinusoidal signal trace with constant amplitude and period equal to λ/4 (λ, excitation wavelength) confirmed an accurate calibration and proper functioning of the mirror segment. The same was repeated for all DM segments. Tip and tilt displacement was verified by recording the image of a 10-μm diameter fluorescent bead while scanning a single DM segment along the maximum tip and tilt range. The light reflected off the remaining segments was blocked by the field stop. Using a custom-written MATLAB code, the centroid of the bead was determined for each tip and tilt position, and a plot of measured vs. expected tip and tilt was calculated, taking into consideration the magnification factors in our microscope setup. A slope approximately equal to 1 confirmed accurate calibration of the mirror segment. The same was repeated for all remaining segments. The settling times of the mirror segments were found to be < 100 μs, which allowed us to carry out kHz modulation of the light impinging on it.

Supplementary Note 2: Modulation strategies

Two different modulation strategies were used during the aberration measurement procedure: phase modulation and intensity modulation. During phase modulation, mirror segments were piston-displaced between -π/2 and π/2 (imparting the beamlets reflecting off them a phase shift ranging from -π to π) at frequency ω_s, resulting in a modulation on the detected fluorescence signal. During intensity modulation, a large tip (or tilt) angle was intermittently applied to the mirror segments being modulated, each at a unique ω_s, such that the beamlets impinging on them alternate between two positions: the "on" position, where beamlets went through the field stop placed after the DM; and the "off" position, where beamlets were blocked by the field stop (Supplementary Fig. 9).

During phase modulation, the modulation in the fluorescence signal originates from the varying phase offsets between the modulated rays and the reference focus. In contrast, during intensity modulation, the periodic variation in the fluorescence signal comes from the changes in excitation power at the focal plane. While for phase modulation there is always a maximum present in 2D maps of interference strength versus displacement, for intensity modulation, if the relative phase between the ray and the reference focus is near π/2, a clear maximum would be absent from the resulting map, in which case a π/2 phase offset needs to be added to the corresponding segment and the measurement redone.

Depending on the sample, fluorescent features of different sizes may be used for aberration measurement. We systematically tested and compared the performance of phase versus intensity modulation, each of which was used to measure artificial aberrations using the signal from fluorescent features of different sizes (Extended Data Fig. 2). Experimentally we found that, for 2P microscopy, phase modulation outperformed intensity modulation when signal from small features (< 4 µm) was used for aberration measurement, whereas intensity modulation led to faster improvement of image quality for features larger than 4 µm. For 3P microscopy, phase modulation was found to perform better than or equally with intensity modulation for all feature sizes tested (from 1-µm diameter fluorescent beads to a fluorescent solution). Similar performance between phase and intensity modulation was validated *in vivo* by performing the correction using a neuronal cell body (Extended Data Fig. 6).

Supplementary Note 3: Phase offset measurement

Mathematically, the phase offset measurement can be understood as follows[3]: the modulated and reference rays interfere at the focus, modulating the focal intensity and thus the resulting 2P/3P fluorescence signal. The electric field at the focus can be written as:

$$E(t) = E_r e^{i(\omega t+\theta_r)} + \sum_{s=1}^{N} E_s e^{i(\omega t+\omega_s t+\theta_s)},$$

where E_r and E_s are the amplitudes of the reference and modulated (corresponding to segment s) electric fields, respectively; θ_r and θ_s are the phases of the reference and modulated electric fields, respectively; ω is the angular frequency of the electric field; ω_s is the angular frequency of the phase modulation for segment s; and N is the total number of modulated segments (for our mirror, 20 for the first group, and 17 for the second).

The intensity at the focus is $I(t) = |E(t)|^2$ and, using the previous equation, can be written as:

$$I(t) = E_r^2 + 2E_r \sum_{s=1}^{N} E_s \cos(\omega_s t + \theta_s - \theta_r) + \sum_{s=1}^{N} E_s^2 + M(t),$$

where $M(t)$ contains interference terms between the different modulated segments, which, when ω_s's are chosen carefully, results in a modulation of the focal intensity at frequencies distinct from ω_s's. Lastly, the fluorescence signal is $S(t) \propto I(t)^m$, with $m = 2{,}3$ for 2P and 3P excitation, respectively. In either case it can be shown that:

$$S(t) = \sum_{s=1}^{N} C_s \cos(\omega_s t + \theta_s - \theta_r) + B(t) + A,$$

where C_s are constant values unique to each segment and dependent on $E_r, E_s, \text{and } \sum_{s=1}^{N} E_s^2$, A is time-independent, and $B(t)$ is modulated at frequencies different than ω_s's. Taking the Fourier transform of the fluorescence trace $S(t)$, the phase value at ω_s is $\theta_r - \theta_s$, the phase offset leading to constructive interference between the reference and modulated ray on segment s.

Supplementary Note 4: Immunohistochemistry to assess tissue injury after running AO routine

Following previously used protocols[4,5] we immunolabeled postmortem mouse brain slices (Supplementary Fig. 7) against early markers of tissue injury (heat shock protein and microglial activation). Briefly, our AO routine was performed 3 weeks after cranial window implantation on wild-type mice (C57BL/6J), using the same power, integration time, number of iterations, and imaging depth as the example shown in Fig. 2a,b. We had a second mouse as a control (same age and sex), which had undergone the same cranial window implantation procedure on the same day as the first mouse but was never exposed to laser light. 17 hours after performing the AO routine, both mice were perfused with 4% paraformaldehyde in 1x PBS and their brains postfixed in this solution for ~24 hours, and then in 30% (w/V) sucrose in 1x PBS for another ~24 hours until they sank to the bottom of the tube. Relevant brain regions (e.g., exposed to laser light through the center of the cranial window) were coronally sectioned into 50 μm sections and incubated with primary antibodies for 16 hours. Alternating slices were labeled for heat shock protein (anti-HSP70/72, mouse monoclonal, 1:400 dilution, Enzo Life Sciences, Part # SPA-810PE-D) and microglial activation (anti-Iba1, rabbit, polyclonal, 1:1000 dilution, WAKO, Part # 019-19741). Slices were washed 3 times for 10 min each in 1x PBS and incubated with a species appropriate secondary antibody (donkey, 1:2000 dilution, Invitrogen, Part #s A-31573 and A-31571) conjugated to Alexa Fluor 647 for 2 hours. Slices were washed 3 times in 1x PBS, stained with Hoechst nuclear stain for 10 minutes and mounted for imaging using an Olympus VS120 automatic slide scanner. We performed similar experiments on a mouse spinal cord (Supplementary Fig. 8). Given our current acute protocol for spinal cord imaging, we performed the perfusion on the same day as the surgery and 5 hours after the AO routine was run.

References

1. Stewart, J. B. *et al.* Design and development of a 331-segment tip-tilt-piston mirror array for space-based adaptive optics. *Sensors Actuators, A Phys.* **138**, 230–238 (2007).
2. Stewart, J. B., Diouf, A., Zhou, Y. & Bifano, T. G. Open-loop control of a MEMS deformable mirror for large-amplitude wavefront control. *J. Opt. Soc. Am. A* **24**, 3827 (2007).
3. Liu, R., Milkie, D. E., Kerlin, A., MacLennan, B. & Ji, N. Direct phase measurement in zonal wavefront reconstruction using multidither coherent optical adaptive technique. *Opt. Express* **22**, 1619–1628 (2014).
4. Podgorski, K. & Ranganathan, G. Brain heating induced by near-infrared lasers during multiphoton microscopy. *J. Neurophysiol.* **116**, 1012–1023 (2016).
5. Wang, T. *et al.* Quantitative analysis of 1300-nm three-photon calcium imaging in the mouse brain. *Elife* **9**, (2020).